AGU ADVANCING EARTH AND SPACE SCIENCE

Geophysical Research Letters

RESEARCH LETTER
10.1029/2020GL089630

Special Section:
InSight at Mars

Autocorrelation Reflectivity of Mars

Sizhuang Deng[1] and Alan Levander[1]

[1]Department of Earth, Environmental and Planetary Sciences, Rice University, Houston, TX, USA

Abstract The seismic structure of the Martian interior can shed light on the formation and dynamic evolution of the planet and our solar system. The deployment of the seismograph carried by the InSight mission provides a means to study Martian internal structure. We used ambient noise autocorrelation to analyze the available vertical component seismic data to recover the reflectivity beneath the Insight lander. We identify the noise that is approximately periodic with the Martian sol as daily lander operations and the diurnal variation in Martian weather and tides. To investigate the seismic discontinuities at different depths, the autocorrelograms are filtered and stacked into different frequency bands. We observe prominent reflection signals probably corresponding to the Martian Moho, the olivine-wadsleyite transition in the mantle, and the core-mantle boundary in the stacked autocorrelograms. We estimate the depths of these boundaries as ~35, 1,110–1,170, and 1,520–1,600 km, consistent with other estimates.

Plain Language Summary Knowledge of the Martian interior informs theories for the formation and dynamic evolution of another terrestrial planet, hence providing information on the history of the solar system. On Earth, subsurface structure is discovered by analysis of seismic signals recorded by large seismograph arrays deployed worldwide. The InSight lander carried one seismic station to Mars at the end of 2018, providing the opportunity to investigate the internal structure of Mars. Here we autocorrelated ambient noise from the available seismic data to investigate the subsurface discontinuities of Mars. In the raw seismic data, we observe the long-period signals with a period of ~1 Martian sol (~3% longer than an Earth day), which are related to the diurnal variation in weather and tides. After the removal of instrument response, remaining high-amplitude peaks are likely caused by the daily operations of the InSight lander. We preprocessed the raw data and used different frequency bands to detect discontinuities at different depths. We identify prominent signals in the stacked autocorrelation reflectivity as likely originating from the Martian Moho, the olivine-wadsleyite transition in the Martian mantle, and the core-mantle boundary. These results are consistent with other observations and measurements.

Key Points:
- Autocorrelation analysis of SEIS data shows signals probably from the Martian Moho, olivine-wadsleyite transition, and core-mantle boundary
- Depth conversion of these signals gives discontinuity depths consistent with estimates made with other methods
- A high crustal Vp/Vs ratio suggests the composition of Martian crust is composed of basaltic and andesitic rocks

Supporting Information:
- Supporting Information S1

Correspondence to:
S. Deng,
sd62@rice.edu

Citation:
Deng, S., & Levander, A. (2020). Autocorrelation reflectivity of Mars. *Geophysical Research Letters*, *47*, e2020GL089630. https://doi.org/10.1029/2020GL089630

Received 22 JUL 2020
Accepted 23 JUL 2020
Accepted article online 4 AUG 2020

1. Introduction

The InSight seismograph (Seismic Experiment of Internal Structure [SEIS]) gives us the ability to investigate the interior structure of another inner planet in the solar system (Smrekar et al., 2019). Martian subsurface structures have been studied at different scales during past decades by gravity anomaly inversion (Kiefer et al., 1996; Neumann et al., 2004; Parro et al., 2017; Zuber et al., 2000), solar tide detection (Yoder et al., 2003), high-pressure experiments (Bertka & Fei, 1997; Fei, 2013; Stewart et al., 2007), and thermoelastic model calculation and inversion (Khan et al., 2018; Khan & Connolly, 2008; Rivoldini et al., 2011; Sohl & Spohn, 1997; Zharkov et al., 2009). Mars, with a similar interior structure to Earth, can be divided into crust, mantle, and core (Smrekar et al., 2019). The Viking 2 seismic recordings provided modest information on the interior structure of the planet (Anderson et al., 1977) which has led to numerical and theoretical estimation of seismic properties prior to the InSight mission (Lognonné et al., 2019; Panning et al., 2017). Hundreds of Mars-quakes have been recorded by the SEIS instrument (Banerdt et al., 2020; Giardini et al., 2020; Lognonné et al., 2020). Estimates of crustal thickness have been made from gravity observations, which among other observations suggest a dichotomy between the northern and southern hemispheres (Genova et al., 2016; Parro et al., 2017; Zuber, 2001). Evidence that Mars' core is largely liquid has been demonstrated by the large k_2 Love number (Rivoldini et al., 2011; Yoder et al., 2003) and high-pressure experiments using assumed core properties (Stewart et al., 2007), while the existence of a solid inner core is still unknown.

Claerbout (1968) showed that the reflectivity series of an acoustic media can be recovered by taking the autocorrelation of the normal-incidence transmission response, a form of seismic interferometry, that was subsequently extended to elastic media and nonnormal incidence angles by Frasier (1970). Body-wave

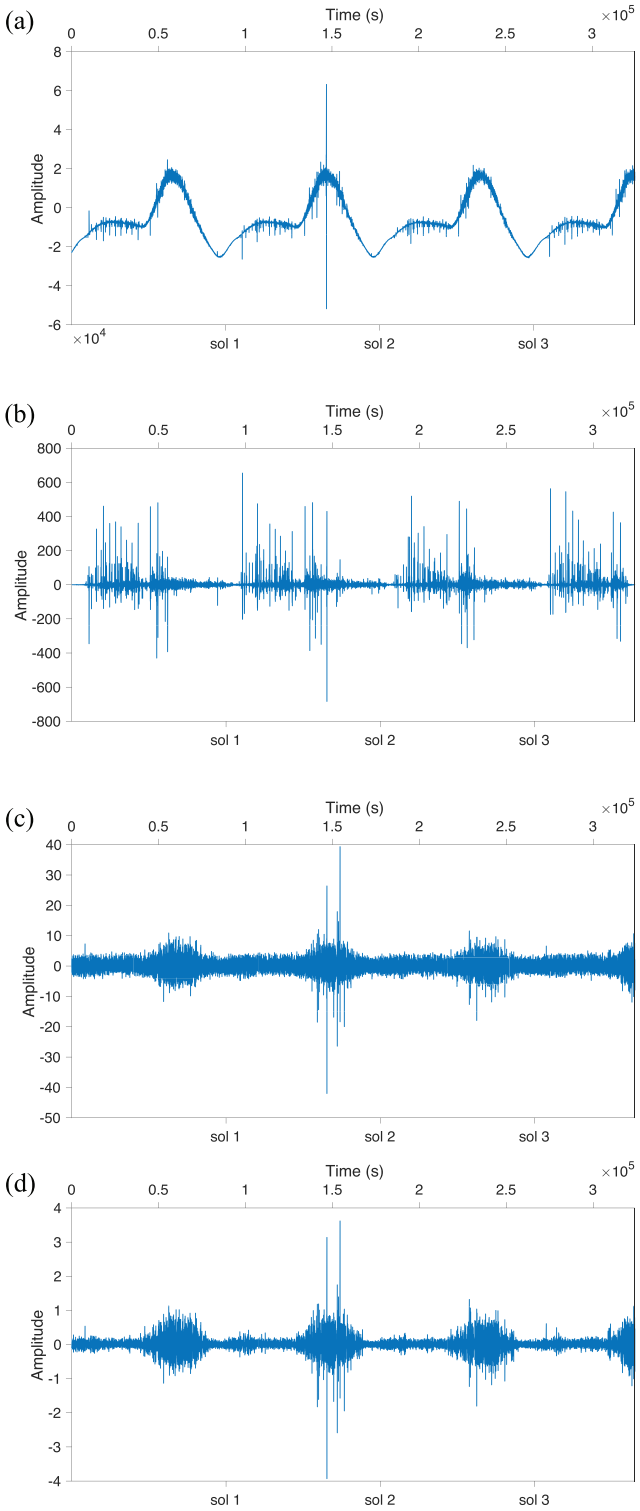

Figure 1. (a) The raw Z-component data with instrument response. The data are recorded from 26 to 29 April 2019 (~3.7 sols). (b) The Z-component data after the removal of instrument response and band-pass filter between 0.01 and 3.5 Hz. (c) The Z-component data at the same period after temporal balance. (d) The Z-component data at the same period after spectral whitening.

reflection phases have been successfully extracted by cross-correlating (Clayton, 2020; Feng et al., 2017; Lin & Tsai, 2013; Roux et al., 2005; Tkalčić & Pham, 2018; Zhan et al., 2010) and autocorrelating (Becker & Knapmeyer-Endrun, 2018, 2019; Phạm & Tkalčić, 2018; Romero & Schimmel, 2018) the seismic wavefield. Most recent studies have focused on the extraction of Moho-reflected phases (e.g., PmP and SmS) to determine crustal thickness by autocorrelating and stacking the ambient noise record (Gorbatov et al., 2013; Oren & Nowack, 2017; Tibuleac & von Seggern, 2012) or teleseismic earthquake data (Delph et al., 2019; Phạm & Tkalčić, 2017). Besides the Moho discontinuity, stacked ambient noise autocorrelations have been used to study the reflectivity of the lithosphere and lithosphere-asthenosphere boundary (Kennett, 2015; Kennett & Sippl, 2018). The cross-correlation of continuous noise data (Lin et al., 2013) and autocorrelation of earthquake coda waves (Wang et al., 2015) have been used to identify core phases.

The successful applications of single-station-based autocorrelation to studying Earth's interior show its potential for determining subsurface structures using the single seismometer available on Mars. In this work we calculated and stacked the Z-component autocorrelograms to determine the depth of subsurface interfaces beneath the SEIS station using the continuously recorded ambient noise data. The reflection responses at different depths are identified by applying different band-pass filters to the seismic data. We depth convert the reflection sequence in time using theoretical models of the 1-D Martian interior to provide approximate depths to Martian seismic discontinuities.

2. Data and Methods

The InSight ambient noise seismic data were downloaded from Incorporated Research Institutions for Seismology data center in BHU-V-W channels. The data, sampled at 10 Hz, were collected by SEIS from February thru August 2019, where the instruments were protected by the wind and thermal shield to reduce noise (Lognonné et al., 2019). Preprocessing included removing the instrument response from the raw continuous data followed by band-pass filtering from 0.01 to 3.5 Hz. The data were then cut into approximately one thousand one hundred 2-hr windows and rotated into Z-N-E components based on the dip and azimuth information of U-V-W channels. We removed the mean and trend and tapered each 2-hr-long window using the Tukey window with cosine fraction of 0.02. Figure 1a shows the ~3.7-sol long raw Z-component waveform sample, where the low-frequency signals may correspond to the diurnal weather and tidal variation. Figure 1b is the Z-component waveform after the removal of instrument response and filtering from 0.01 to 3.5 Hz. The high-frequency spikes (Figures 1b and S2 in the supporting information) are probably generated by lander operations during a Martian sol. To suppress these features, we applied a temporal balance (Bensen et al., 2007) using a running absolute mean normalization to eliminate the effects of nonstationary noise before making the autocorrelograms. The weighting function $w(t)$ used to normalize the trace $s(t)$ is defined as

$$w(t) = \frac{1}{\frac{1}{2N+1}\sum_{t-N\Delta t \le \tau \le t+N\Delta t}|s(\tau)|},$$

where $2N\Delta t$ is the parameter to control the length of moving-average windows. In this paper, we will calculate the weighting function using 100-s moving-average window to normalize the seismic data. The Z-component waveform with temporal balance is shown in Figure 1c, illustrating that the energetic peaks are significantly diminished compared with the original trace in Figure 1b. We also compared the autocorrelation results using the ambient noise data from only the Martian night, which lacks the high amplitude spikes, and autocorrelations made from data recorded during the Martian day (Figures S3 and S4).

Compared to broadband seismic data on Earth, the InSight data contain much more low-frequency energy. A spectral whitening method (Bensen et al., 2007; Oren & Nowack, 2017; Phạm & Tkalčić, 2017, 2018) is applied to each 2-hr-long data window to remove the low-frequency bias and boost the high-frequency component (Figure 1d), where the whitening width is empirically determined as 0.5 Hz (Phạm & Tkalčić, 2017). The application of spectral whitening will make the reflection phases more pronounced and interpretable (Delph et al., 2019; Phạm & Tkalčić, 2017). The autocorrelograms are computed and normalized by the maximum amplitude at zero lag for each trace. In order to boost the coherent signals of each trace and suppress the noise, a linear phase-weighted stacking (PWS) method (Schimmel & Paulssen, 1997) was applied to the sum of autocorrelation windows. We chose the linear weight empirically, based on the trade-off between the coherency measure and waveform distortion. Lastly, we sum all of the 2-hr autocorrelation windows, producing two autocorrelation estimates, one with and one without phase weighting. We followed the same processing steps to calculate the autocorrelations for purely random signals, indicating no bias is introduced to the autocorrelation series by the processing sequence (Figure S1).

In order to recover the seismic discontinuities throughout the depths of Mars (ranging from tens of km to >1,000 km), we applied different band-pass filters: Overlapping Butterworth band-pass filters in the high-frequency range (0.625–3.0 Hz) show what we interpret to be the Moho discontinuity, whereas low-frequency (0.05–0.2 Hz) overlapping filters show what we interpret to be the mantle olivine-wadsleyite transition and the core-mantle boundary. We also examined different frequency bands to determine the robustness of the observed seismic phases. After stacking and filtering, we converted the resulting autocorrelograms from time to depth using the *P* wave velocity models derived from the joint inversion of multiple geophysical data (Khan et al., 2018) and mineralogical simulations (Panning et al., 2017; Yoshizaki & McDonough, 2020).

3. Results and Discussion

3.1. Moho Discontinuity

The high-frequency filtered ambient noise data show prominent reflection phases at ~11.5 (Phase 1) and ~21.0 s (Phase 2) across several frequency bands in both the PWS stack (Figure 2a) and the linear stack (Figure S5). The signal at ~6 s blends into the autocorrelation 0-lag side lobes (Figure 2a), so we will not interpret this event as a reflection phase from Martian interior. Bootstrap calculations suggest the phase identification is robust (Figure S6). The autocorrelation test using the data without high amplitude spikes produces identical autocorrelation results (Figure S3), indicating the observations of the reflection phases are reliable. These events can be interpreted a number of different ways. (1) The first phase could be PmP, the *P* wave Moho reflection, and the second the SmS phase (Figure 2a). SmS can be observed on a vertical component, because the recorded noise incidence angles actually form a narrow cone around vertical rather than arriving only vertically (Gorbatov et al., 2013; Oren & Nowack, 2017; Phạm & Tkalčić, 2017). (2) Phase 1 could be PmP, while the second phase could be the multiple of the first event, PmP2, since the arrival of the second event is close to double the time of Phase 1. (3) Phase 1 could be PmP, with Phase 2 an event from the upper mantle. (4) The first phase might be an intracrustal event analogous to the Conrad discontinuity and the second phase the Moho.

Using a *P* wave crustal velocity model (LFAK) for a gabbroic crust shown in Figure 2b (Khan et al., 2018), the first three models give a crustal thickness of ~35-km depth (Figure 2c). The crustal thickness of ~35 km is 30 km shallower than that in the LFAK velocity model (Figure 2b). One possible interpretation is that the Moho depth (~65 km) of LFAK velocity model represents the average of the thin crust of Martian northern hemisphere (~30–40 km) and the thick crust (~70–80 km) of the southern hemisphere, while the autocorrelation reflectivity series in our study measure local crustal thickness beneath the InSight lander. The global Martian crustal thickness map inverted from gravity data (Genova et al., 2016; Parro et al., 2017; Zuber

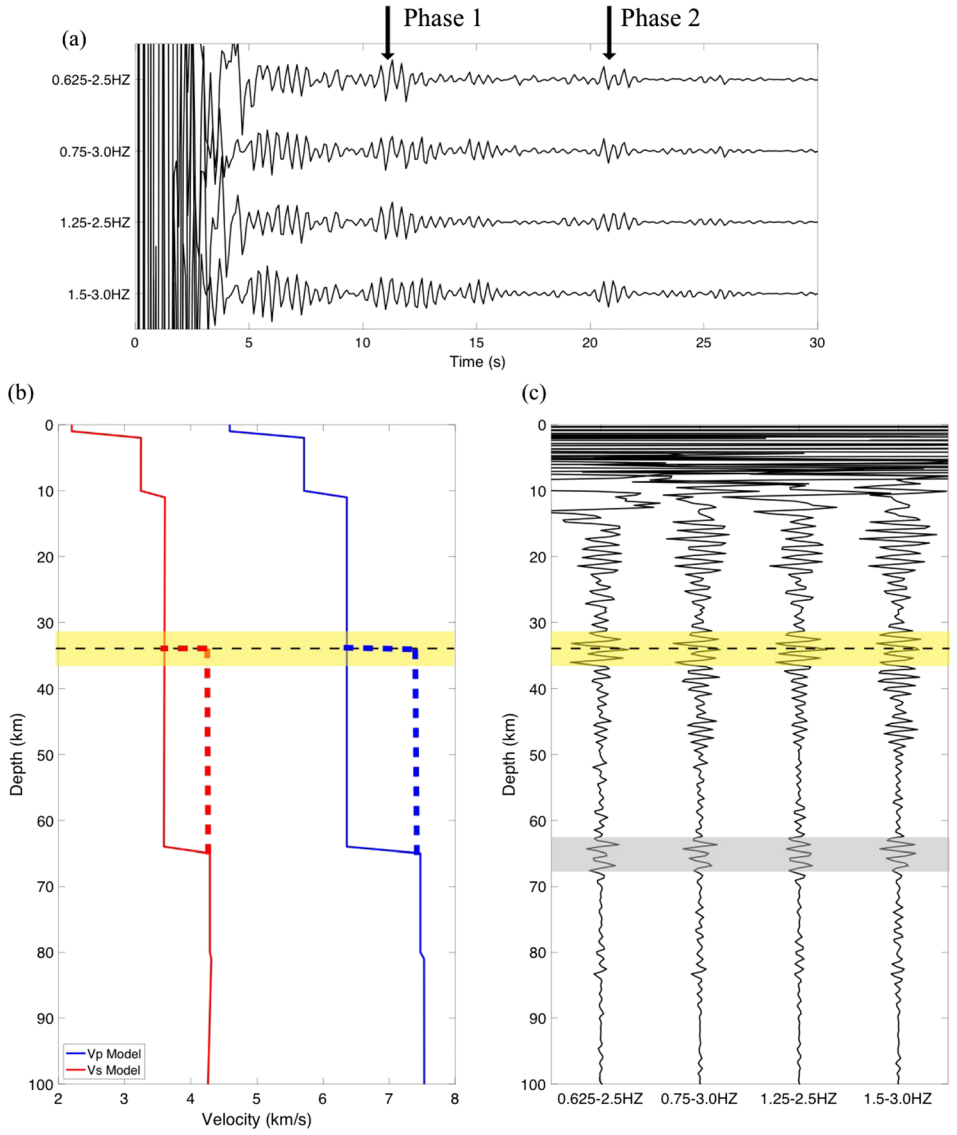

Figure 2. (a) The PWS stacked autocorrelograms filtered into different high-frequency bands. Arrivals at ~11.5 (Phase 1) and at ~21 s (Phase 2) are marked as black arrows. The arrivals can be interpreted as the Moho reflections PmP and SmS (Model 1), as PmP and PmP2 (Model 2), as PmP and an upper mantle discontinuity (Model 3), or as an intracrustal event and PmP (Model 4). (b) The *P* (blue solid line) and *S* wave (red solid line) velocity model (LFAK) (solid line) derived from the joint inversion of multiple geophysical data (Khan et al., 2018). The dashed lines at ~35 km represent the crustal thickness beneath the InSight lander derived from autocorrelation reflectivity series if Models 1–3 are assumed. (c) Depth conversion of the autocorrelation reflectivity using the *P* wave velocity model in (b). The yellow shaded area at ~35 km represents the interpreted Martian Moho for Models 1–3 or the intracrustal discontinuity for Model 4. The gray shaded area does not have physical meaning if Phase 2 is interpreted as SmS for Model 1 or PmP2 for Model 2. The gray shaded area at ~68 km corresponds to the depth of upper mantle discontinuity for Model 3 or the Martian Moho for Model 4. We prefer Model 1.

et al., 2000) shows a crustal thickness of 30–35 km at the InSight lander site, close to the 35 km estimated for the first event being PmP.

Assuming the second event is SmS, the Vp/Vs ratio is estimated from the *S* and *P* wave reflection traveltimes, namely,

$$\frac{V_p}{V_s} = \frac{T(SmS)}{T(PmP)} \approx 1.83,$$

which is compatible with the Vp/Vs ratio for basaltic and andesitic rocks (~1.84) (Christensen, 1996). Thermal emission spectral analysis of the Martian surface (McSween et al., 2003, 2009) and geological observations (Golombek et al., 2020) suggests that the Martian crust is andesitic and basaltic. The Vp/Vs ratio we measure is consistent with that result.

Assuming the second event is from a mantle interface gives a depth of ~68 km or 33 km into the mantle. This could represent an intralithospheric boundary remnant from basalt extraction. The Martian lithosphere has been estimated to be greater than 150 km based on elastic modeling (Grott & Breuer, 2010; Schumacher & Breuer, 2006; Thurber & Toksöz, 1978); hence, the second event is unlikely to represent the Martian lithosphere-asthenosphere boundary.

The fourth interpretation gives a crustal thickness of ~68 km and an intracrustal horizon at ~35 km. We would interpret the first event as the boundary between an intermediate and mafic crust.

Given the gravity estimates of crustal thickness and the Vp/Vs ratio being close to that expected for a gabbroic crust, we favor the interpretation that the 11.5-s event is PmP and the 21-s event is SmS.

3.2. Deeper Interior: Olivine-Wadsleyite Transition and Core-Mantle Boundary

We observe two prominent events in the low-frequency band of both the PWS (Figure 3a) and the linear stack (Figure S7) autocorrelograms, the first at ~280 s and the second at ~375 s. These two phases are also clearly observed in bootstrap calculations (Figure S8), further demonstrating the reliability of the phase identification using different subsets of data. The autocorrelation series made with the nighttime data without high amplitude spikes also shows these events clearly (Figure S4). That lower-frequency signals from deep within Mars are observable is not too surprising, as Mars is a cold, dry planet, and seismic attenuation is strongly dependent on temperature and on the fluid content of rocks. We use four *P* wave velocity models (Figure 3b) to depth convert the stacked autocorrelograms, one is the LFAK model (Khan et al., 2018), three are from theoretical calculation of shear wave velocity for various bulk composition and thermal state models (Panning et al., 2017) where we assume a Vp/Vs ratio of 1.82 (Sohl & Spohn, 1997), and one is from a theoretical calculation of Vp (Yoshizaki & McDonough, 2020).

Figure 3c shows the depth conversion of the reflectivity series filtered between 0.05 and 0.1 Hz using the four models shown in Figure 3b. We interpret the phase at ~280 s as the reflection from the olivine-wadsleyite transition. Depth conversion using the different Martian seismic velocity models puts this boundary at depths ranging from 1,110 to 1,170 km. The depth of the olivine-wadsleyite phase transition on Mars is expected to be ~2.8 times greater than the corresponding discontinuity on Earth (~410 km), a result of the low gravity and mean density on Mars (gravity: 3.71 m/s^2; mean density: 3.93 g/cm^3) and lower internal temperatures compared with Earth (gravity: 9.81 m/s^2; mean density: 5.51 g/cm^3). The phase we identify as from the olivine-wadsleyite transition matches the results derived from thermodynamic and mineralogical inversion, where the depth of this transition is estimated to be at ~1,100 km (Khan et al., 2018; Khan & Connolly, 2008; Verhoeven et al., 2005; Yoshizaki & McDonough, 2020).

A second prominent event at ~375 s depth converts to 1,520–1,600 km. A thermal model of the mantle (Khan & Connolly, 2008) predicts the Martian mantle would not reach the temperatures and pressures necessary for the ringwoodite-perovskite transition, referred to as the 660 discontinuity on Earth. The mineralogical model suggests that the theoretical depth of the ringwoodite-perovskite transition would occur at ~1,900 km (Breuer et al., 1996); therefore, we interpret the second deep event as the body-wave reflection from the Martian core-mantle boundary, PcP (Figure 3a). Depth conversion with the four velocity models shown in Figure 3b puts the core-mantle boundary in the depth range 1,520–1,600 km (Figure 3c). Since the average radius of Mars is ~3,390 km, we estimate the core radius to be 1,790–1,870 km.

Yoder et al. (2003) estimated the potential Love number k_2, which represents the solar tidal deformation of Mars, to constrain the Martian core radius to be 1,520 to 1,840 km. Rivoldini et al. (2011) inverted geodetic data assuming various mineralogic models and thermal conditions, giving a core radius between 1,700 and 1,900 km. Khan et al. (2018) explored several geophysical observations, such as moment of inertia, mean mass, and tidal response of Mars, to recover the bulk composition and thermal state and estimated the core radius to be 1,730–1,840 km. In general, our measurement of depth to the core-mantle boundary and the core radius is consistent with the results from other types of geophysical data.

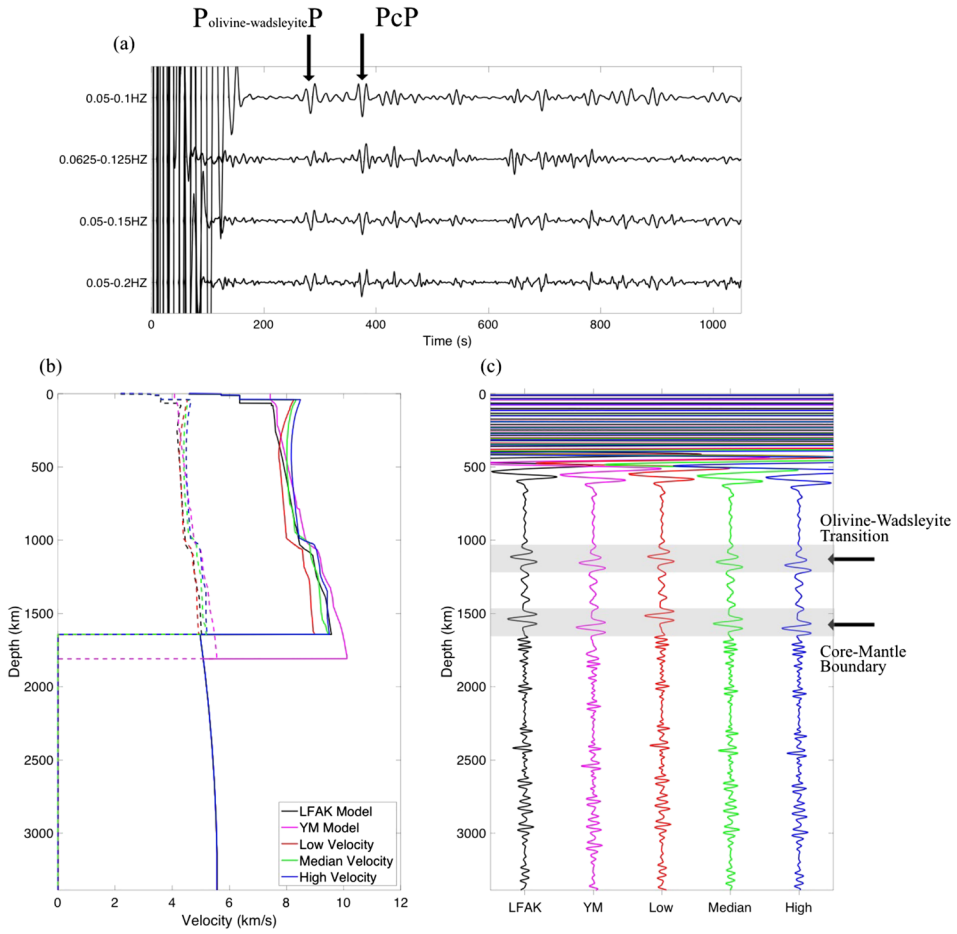

Figure 3. (a) The PWS stacked autocorrelograms filtered into different low-frequency bands. The arrival times expected of the reflection signals from olivine-wadsleyite transition and core-mantle boundary are marked as black arrows. (b) The *P* (solid line) and *S* wave (dashed line) velocity model, LFAK model from the joint inversion of multiple geophysical data (Khan et al., 2018), YM model from theoretical calculation (Yoshizaki & McDonough, 2020), and three representative velocity models from mineralogical simulation (Panning et al., 2017). (c) Depth conversion of stacked autocorrelation reflectivity series filtered between 0.05 and 0.1 Hz using all *P* wave velocity models in (b). The gray shaded area represents the interpreted Martian olivine-wadsleyite transition and core-mantle boundary.

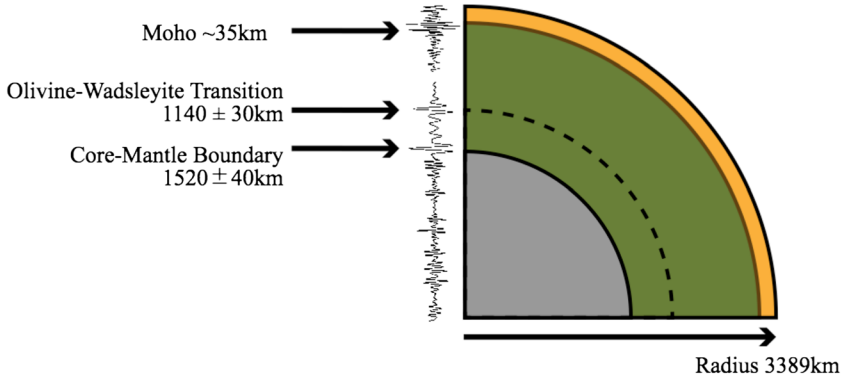

Figure 4. Schema of the Martian interior based on the depth of seismic discontinuities from autocorrelation analysis and assumed velocity models. The yellow, green, and gray regions represent Martian crust, mantle, and core, respectively. The depths of interpreted Moho, olivine-wadsleyite transition, and core-mantle boundary are indicated.

4. Conclusion

Using ambient noise autocorrelation of Martian InSight seismic data, we constructed the reflectivity series beneath the lander. We observe two prominent events from shallow in the Martian interior and two more prominent events from the deeper interior (Figure 4). Crustal, and possibly upper mantle, reflections could be observed in the high-frequency filtered autocorrelation function. Our preferred interpretation is a Martian Moho discontinuity at ~35 km and a Martian crust with Vp/Vs _x0007E; 1.83, suggesting that the Martian crust beneath the lander is mainly basalt or andesite, consistent with the analysis of thermal emission spectra (McSween et al., 2003, 2009). To recover the deeper seismic discontinuities in Mars, we examined low-frequency filtered autocorrelograms which show reflection signals at times consistent for the Martian olivine-wadsleyite transition and the Martian core-mantle boundary. Using different velocity models simulated for various compositional and thermal models (Khan et al., 2018; Panning et al., 2017; Yoshizaki & McDonough, 2020), the olivine-wadsleyite transition and core-mantle boundary of Mars would be at 1,110–1,170 and 1,520–1,600 km, respectively.

Data Availability Statement

The InSight seismic data used in this work were obtained from the Incorporated Research Institutions for Seismology (IRIS) data center (InSight Mars SEIS Data Service, 2019; www.iris.edu/hq/sis/insight).

Acknowledgments

The Department of Earth, Environmental and Planetary Sciences at Rice University supported this research. We thank Valerie Payre for discussions about the interpretation of these data. We thank Editor Jeroen Ritsema, Associate Editor Victor Tsai, and two anonymous reviewers for suggestions that improved the manuscript.

References

Anderson, D. L., Miller, W. F., Latham, G. V., Nakamura, Y., Toksöz, M. N., Dainty, A. M., et al. (1977). Seismology on Mars. *Journal of Geophysical Research*, *82*(28), 4524–4546. https://doi.org/10.1029/js082i028p04524

Banerdt, W. B., Smrekar, S. E., Banfield, D., Giardini, D., Golombek, M., Johnson, C. L., et al. (2020). Initial results from the InSight mission on Mars. *Nature Geoscience*, *13*(3), 183–189. https://doi.org/10.1038/s41561-020-0544-y

Becker, G., & Knapmeyer-Endrun, B. (2018). Crustal thickness across the Trans-European Suture Zone from ambient noise autocorrelations. *Geophysical Journal International*, *212*(2), 1237–1254. https://doi.org/10.1093/gji/ggx485

Becker, G., & Knapmeyer-Endrun, B. (2019). Crustal thickness from horizontal component seismic noise auto- and cross-correlations for stations in Central and Eastern Europe. *Geophysical Journal International*, *218*(1), 429–445. https://doi.org/10.1093/gji/ggz164

Bensen, G. D., Ritzwoller, M. H., Barmin, M. P., Levshin, A. L., Lin, F., Moschetti, M. P., et al. (2007). Processing seismic ambient noise data to obtain reliable broad-band surface wave dispersion measurements. *Geophysical Journal International*, *169*(3), 1239–1260. https://doi.org/10.1111/j.1365-246X.2007.03374.x

Bertka, C. M., & Fei, Y. (1997). Mineralogy of the Martian interior up to core-mantle boundary pressures. *Journal of Geophysical Research*, *102*(B3), 5251–5264. https://doi.org/10.1029/96jb03270

Breuer, D., Zhou, H., Yuen, D. A., & Spohn, T. (1996). Phase transitions in the Martian mantle: Implications for the planet's volcanic history. *Journal of Geophysical Research*, *101*(E3), 7531–7542. https://doi.org/10.1029/96JE00117

Christensen, N. I. (1996). Poisson's ratio and crustal seismology. *Journal of Geophysical Research*, *101*(B2), 3139–3156. https://doi.org/10.1029/95jb03446

Claerbout, J. F. (1968). Synthesis of a layered medium from its acoustic transmission response. *Geophysics*, *33*(2), 264–269. https://doi.org/10.1190/1.1439927

Clayton, R. W. (2020). Imaging the subsurface with ambient noise autocorrelations. *Seismological Research Letters.*, *91*(2A), 930–935. https://doi.org/10.1785/0220190272

Delph, J. R., Levander, A., & Niu, F. (2019). Constraining crustal properties using receiver functions and the autocorrelation of earthquake-generated body waves. *Journal of Geophysical Research: Solid Earth*, *124*, 8981–8997. https://doi.org/10.1029/2019JB017929

Fei, Y. (2013). Simulation of the planetary interior differentiation processes in the laboratory. *Journal of Visualized Experiments: JoVE*, (81), e50778. https://doi.org/10.3791/50778

Feng, J., Yao, H., Poli, P., Fang, L., Wu, Y., & Zhang, P. (2017). Depth variations of 410 km and 660 km discontinuities in eastern North China Craton revealed by ambient noise interferometry. *Geophysical Research Letters*, *44*, 8328–8335. https://doi.org/10.1002/2017GL074263

Frasier, C. W. (1970). Discrete time solution of plane P-SV waves in a plane layered medium. *Geophysics*, *35*(2), 197–219. https://doi.org/10.1190/1.1440085

Genova, A., Goossens, S., Lemoine, F. G., Mazarico, E., Neumann, G. A., Smith, D. E., & Zuber, M. T. (2016). Seasonal and static gravity field of Mars from MGS, Mars Odyssey and MRO radio science. *Icarus*, *272*, 228–245. https://doi.org/10.1016/j.icarus.2016.02.050

Giardini, D., Lognonné, P., Banerdt, W. B., Pike, W. T., Christensen, U., Ceylan, S., et al. (2020). The seismicity of Mars. *Nature Geoscience*, *13*(3), 205–212. https://doi.org/10.1038/s41561-020-0539-8

Golombek, M., Warner, N. H., Grant, J. A., Hauber, E., Ansan, V., Weitz, C. M., et al. (2020). Geology of the InSight landing site on Mars. *Nature Communications*, *11*(1), 1014–1011. https://doi.org/10.1038/s41467-020-14679-1

Gorbatov, A., Saygin, E., & Kennett, B. L. N. (2013). Crustal properties from seismic station autocorrelograms. *Geophysical Journal International*, *192*(2), 861–870. https://doi.org/10.1093/gji/ggs064

Grott, M., & Breuer, D. (2010). On the spatial variability of the martian elastic lithosphere thickness: Evidence for mantle plumes? *Journal of Geophysical Research*, *115*, E03005. https://doi.org/10.1029/2009JE003456

InSight Mars SEIS Data Service. (2019). SEIS raw data, Insight Mission. IPGP, JPL, CNES, ETHZ, ICL, MPS, ISAE-Supaero, LPG, MFSC. https://doi.org/10.18715/SEIS.INSIGHT.XB_2016

Kennett, B. L. N. (2015). Lithosphere-asthenosphere P-wave reflectivity across Australia. *Earth and Planetary Science Letters*, *431*, 225–235. https://doi.org/10.1016/j.epsl.2015.09.039

Kennett, B. L. N., & Sippl, C. (2018). Lithospheric discontinuities in Central Australia. *Tectonophysics*, *744*, 10–22. https://doi.org/10.1016/j.tecto.2018.06.008

Khan, A., & Connolly, J. A. D. (2008). Constraining the composition and thermal state of Mars from inversion of geophysical data. *Journal of Geophysical Research*, *113*, E07003. https://doi.org/10.1029/2007JE002996

Khan, A., Liebske, C., Rozel, A., Rivoldini, A., Nimmo, F., Connolly, J. A. D., et al. (2018). A geophysical perspective on the bulk composition of Mars. *Journal of Geophysical Research: Planet*, *123*, 575–611. https://doi.org/10.1002/2017JE005371

Kiefer, W. S., Bills, B. G., & Steven Nerem, R. (1996). An inversion of gravity and topography for mantle and crustal structure on Mars. *Journal of Geophysical Research*, *101*(E4), 9239–9252. https://doi.org/10.1029/95JE03699

Lin, F. C., & Tsai, V. C. (2013). Seismic interferometry with antipodal station pairs. *Geophysical Research Letters*, *40*, 4609–4613. https://doi.org/10.1002/grl.50907

Lin, F. C., Tsai, V. C., Schmandt, B., Duputel, Z., & Zhan, Z. (2013). Extracting seismic core phases with array interferometry. *Geophysical Research Letters*, *40*, 1049–1053. https://doi.org/10.1002/grl.50237

Lognonné, P., Banerdt, W. B., Giardini, D., Pike, W. T., Christensen, U., Laudet, P., et al. (2019). SEIS: Insight's Seismic Experiment for Internal Structure of Mars. *Space Science Reviews*, *215*(1), 12. https://doi.org/10.1007/s11214-018-0574-6

Lognonné, P., Banerdt, W. B., Pike, W. T., Giardini, D., Christensen, U., Garcia, R. F., et al. (2020). Constraints on the shallow elastic and anelastic structure of Mars from InSight seismic data. *Nature Geoscience*, *13*(3), 213–220. https://doi.org/10.1038/s41561-020-0536-y

McSween, H. Y., Grove, T. L., & Wyatt, M. B. (2003). Constraints on the composition and petrogenesis of the Martian crust. *Journal of Geophysical Research*, *108*(E12), 5135. https://doi.org/10.1029/2003je002175

McSween, H. Y., Jeffrey Taylor, G., & Wyatt, M. B. (2009). Elemental composition of the Martian crust. *Science*, *324*(5928), 736–739. https://doi.org/10.1126/science.1165871

Neumann, G. A., Zuber, M. T., Wieczorek, M. A., McGovern, P. J., Lemoine, F. G., & Smith, D. E. (2004). Crustal structure of Mars from gravity and topography. *Journal of Geophysical Research*, *109*, E08002. https://doi.org/10.1029/2004JE002262

Oren, C., & Nowack, R. L. (2017). Seismic body-wave interferometry using noise autocorrelations for crustal structure. *Geophysical Journal International*, *208*(1), 321–332. https://doi.org/10.1093/gji/ggw394

Panning, M. P., Lognonné, P., Bruce Banerdt, W., Garcia, R., Golombek, M., Kedar, S., et al. (2017). Planned products of the Mars structure service for the InSight Mission to Mars. *Space Science Reviews*, *211*(1-4), 611–650. https://doi.org/10.1007/s11214-016-0317-5

Parro, L. M., Jiménez-Díaz, A., Mansilla, F., & Ruiz, J. (2017). Present-day heat flow model of Mars. *Scientific Reports*, *7*(1), 45629. https://doi.org/10.1038/srep45629

Phạm, T. S., & Tkalčić, H. (2017). On the feasibility and use of teleseismic P wave coda autocorrelation for mapping shallow seismic discontinuities. *Journal of Geophysical Research: Solid Earth*, *122*, 3776–3791. https://doi.org/10.1002/2017JB013975

Phạm, T. S., & Tkalčić, H. (2018). Antarctic ice properties revealed from teleseismic P wave coda autocorrelation. *Journal of Geophysical Research: Solid Earth*, *123*, 7896–7912. https://doi.org/10.1029/2018JB016115

Rivoldini, A., Van Hoolst, T., Verhoeven, O., Mocquet, A., & Dehant, V. (2011). Geodesy constraints on the interior structure and composition of Mars. *Icarus*, *213*(2), 451–472. https://doi.org/10.1016/j.icarus.2011.03.024

Romero, P., & Schimmel, M. (2018). Mapping the basement of the Ebro Basin in Spain with seismic ambient noise autocorrelations. *Journal of Geophysical Research: Solid Earth*, *123*, 5052–5067. https://doi.org/10.1029/2018JB015498

Roux, P., Sabra, K. G., Gerstoft, P., Kuperman, W. A., & Fehler, M. C. (2005). P-waves from cross-correlation of seismic noise. *Geophysical Research Letters*, *32*, L19303. https://doi.org/10.1029/2005GL023803

Schimmel, M., & Paulssen, H. (1997). Noise reduction and detection of weak, coherent signals through phase-weighted stacks. *Geophysical Journal International.*, *130*(2), 497–505. https://doi.org/10.1111/j.1365-246X.1997.tb05664.x

Schumacher, S., & Breuer, D. (2006). Influence of a variable thermal conductivity on the thermochemical evolution of Mars. *Journal of Geophysical Research*, *111*(E2), E02006. https://doi.org/10.1029/2005JE002429

Smrekar, S. E., Lognonné, P., Spohn, T., Banerdt, W. B., Breuer, D., Christensen, U., et al. (2019). Pre-mission InSights on the interior of Mars. *Space Science Reviews*, *215*(1), 3. https://doi.org/10.1007/s11214-018-0563-9

Sohl, F., & Spohn, T. (1997). The interior structure of Mars: Implications from SNC meteorites. *Journal of Geophysical Research*, *102*(E1), 1613–1635. https://doi.org/10.1029/96JE03419

Stewart, A. J., Schmidt, M. W., Van Westrenen, W., & Liebske, C. (2007). Mars: A new core-crystallization regime. *Science*, *316*(5829), 1323–1325. https://doi.org/10.1126/science.1140549

Thurber, C. H., & Toksöz, M. N. (1978). Martian lithospheric thickness from elastic flexure theory. *Geophysical Research Letters*, *5*(11), 977–980. https://doi.org/10.1029/GL005i011p00977

Tibuleac, I. M., & von Seggern, D. (2012). Crust-mantle boundary reflectors in Nevada from ambient seismic noise autocorrelations. *Geophysical Journal International*, *189*(1), 493–500. https://doi.org/10.1111/j.1365-246X.2011.05336.x

Tkalčić, H., & Pham, T. S. (2018). Shear properties of Earth's inner core constrained by a detection of J waves in global correlation wavefield. *Science*, *362*(6412), 329–332. https://doi.org/10.1126/science.aau7649

Verhoeven, O., Rivoldini, A., Vacher, P., Mocquet, A., Choblet, G., Menvielle, M., et al. (2005). Interior structure of terrestrial planets: Modeling Mars' mantle and its electromagnetic, geodetic, and seismic properties. *Journal of Geophysical Research*, *110*, E04009. https://doi.org/10.1029/2004JE002271

Wang, T., Song, X., & Xia, H. H. (2015). Equatorial anisotropy in the inner part of Earth's inner core from autocorrelation of earthquake coda. *Nature Geoscience*, *8*(3), 224–227. https://doi.org/10.1038/ngeo2354

Yoder, C. F., Konopliv, A. S., Yuan, D. N., Standish, E. M., & Folkner, W. M. (2003). Fluid core size of Mars from detection of the solar tide. *Science*, *300*(5617), 299–303. https://doi.org/10.1126/science.1079645

Yoshizaki, T., & McDonough, W. F. (2020). The composition of Mars. *Geochimica et Cosmochimica Acta*, *273*, 137–162. https://doi.org/10.1016/j.gca.2020.01.011

Zhan, Z., Ni, S., Helmberger, D. V., & Clayton, R. W. (2010). Retrieval of Moho-reflected shear wave arrivals from ambient seismic noise. *Geophysical Journal International*, no. https://doi.org/10.1111/j.1365-246X.2010.04625.x

Zharkov, V. N., Gudkova, T. V., & Molodensky, S. M. (2009). On models of Mars' interior and amplitudes of forced nutations. 1. The effects of deviation of Mars from its equilibrium state on the flattening of the core-mantle boundary. *Physics of the Earth and Planetary Interiors*, *172*(3-4), 324–334. https://doi.org/10.1016/j.pepi.2008.10.009

Zuber, M. T. (2001). The crust and mantle of Mars. *Nature*, *412*(6843), 220–227. https://doi.org/10.1038/35084163

Zuber, M. T., Solomon, S. C., Phillips, R. J., Smith, D. E., Tyler, G. L., Aharonson, O., et al. (2000). Internal structure and early thermal evolution of Mars from Mars global surveyor topography and gravity. *Science*, *287*(5459), 1788–1793. https://doi.org/10.1126/science.287.5459.1788